



Aalborg Universitet

AALBORG UNIVERSITY
DENMARK

Modeling and Evaluation of Stator and Rotor Faults for Induction Motors

Tang, Jing; Chen, Jie; Dong, Kan; Yang, Yongheng; Lv, Haichen; Liu, Zhigang

Published in:
Energies

DOI (link to publication from Publisher):
[10.3390/en13010133](https://doi.org/10.3390/en13010133)

Creative Commons License
CC BY 4.0

Publication date:
2020

Document Version
Publisher's PDF, also known as Version of record

[Link to publication from Aalborg University](#)

Citation for published version (APA):

Tang, J., Chen, J., Dong, K., Yang, Y., Lv, H., & Liu, Z. (2020). Modeling and Evaluation of Stator and Rotor Faults for Induction Motors. *Energies*, 13(1), 1-20. [133]. <https://doi.org/10.3390/en13010133>

General rights

Copyright and moral rights for the publications made accessible in the public portal are retained by the authors and/or other copyright owners and it is a condition of accessing publications that users recognise and abide by the legal requirements associated with these rights.




- Users may download and print one copy of any publication from the public portal for the purpose of private study or research.
- You may not further distribute the material or use it for any profit-making activity or commercial gain
- You may freely distribute the URL identifying the publication in the public portal -

Take down policy

If you believe that this document breaches copyright please contact us at vbn@aub.aau.dk providing details, and we will remove access to the work immediately and investigate your claim.

Article

Modeling and Evaluation of Stator and Rotor Faults for Induction Motors

Jing Tang ¹, Jie Chen ^{1,*}, Kan Dong ², Yongheng Yang ³, Haichen Lv ⁴ and Zhigang Liu ^{1,5}

¹ School of Electrical Engineering, Beijing Jiaotong University, Beijing 100044, China; 15117396@bjtu.edu.cn (J.T.); zhgliu@bjtu.edu.cn (Z.L.)

² China Academy of Railway Sciences Co. Ltd., Beijing 100081, China; dongkan1021@sina.com

³ Department of Energy Technology, Aalborg University, 9220 Aalborg, Denmark; yoy@et.aau.dk

⁴ Beijing Qiansiyu Electric Co. Ltd., Beijing 100082, China; lvhaichen@163.com

⁵ Beijing Engineering Research Center for Electrical Rail Transit, Beijing 100044, China

* Correspondence: jiechen@bjtu.edu.cn; Tel.: +86-131-6129-4848

Received: 5 November 2019; Accepted: 20 December 2019; Published: 26 December 2019



Abstract: The modeling of stator and rotor faults is the basis of the development of online monitoring techniques. To obtain reliable stator and rotor fault models, this paper focuses on dynamic modeling of the stator and rotor faults in real-time, which adopts a multiple-coupled-circuit method by using a winding function approach for inductance calculation. Firstly, the model of the induction machine with a healthy cage is introduced, where a rotor mesh that consists of a few rotor loops and an end ring loop is considered. Then, the stator inter-turn fault model is presented by adding an extra branch with short circuit resistance on the fault part of a stator phase winding. The broken rotor bar fault is then detailed by merging and removing the broken-bar-related loops. Finally, the discrete models under healthy and faulty conditions are developed by using the Tustin transformation for digital implementation. Moreover, the stator and rotor mutual inductances are derived as a function of the rotor position according to the turn and winding functions distribution. Simulations and experiments are performed on a 2.2-kW/380-V/50-Hz three-phase and four-pole induction motor to show the performance of the stator and rotor faults, where the saturation effect is considered in simulations by exploiting the measurements of a no load test. The simulation results are in close agreement with the experimental results. Furthermore, magnitudes of the characteristic frequencies of $2f_1$ in torque and $(1 \pm 2s)f_1$ in current are analyzed to evaluate the stator and rotor fault severity. Both indicate that the stator fault severity is related to the short circuit resistance. Further, the number of shorted turns and the number of continuous broken bars determines the rotor fault severity.

Keywords: motor modeling; stator faults; rotor faults; short circuit; broken rotor bar; winding function approach; saturation effect

1. Introduction

It is reported that 37% of stator faults and 10% of rotor faults occur in induction motors in industry applications [1]. In the early stage, most of the stator faults and rotor faults are caused by turn-to-turn insulation failures [2] and broken bar faults [3], respectively. There are many factors that result in stator and rotor faults, including thermal, mechanical, and environmental stresses. For instance, it was indicated in [4] that the insulation degradation of stator windings is the main cause for stator inter-turn faults, where the thermal stress is the most recognized factor for the ultimate insulation failure [5]. Other reasons such as partial discharges (PD) [5] also lead to the insulation decrease, especially in applications with voltage source inverters. Furthermore, in [5] and [6], it has been illustrated that the rotor faults are developed from manufacturing defects, thermal and mechanical stresses.

The thermal expansion can lead to rotor internal misalignment or shaft bending, which will cause rotor unbalancing [7]. To address the fault issues, stator and rotor fault diagnosis methods based on signal processing technologies, modeling or parameters, and artificial intelligence have been developed in the literature. Nevertheless, to explore the degradation of the induction motor performance and to release the online monitoring, reliable models of stator and rotor faults are of importance.

Accordingly, a stator fault model in steady state was introduced in [8], and however, it is not suitable for the analysis of the dynamic performance. In [9], the stator fault in the natural a-b-c reference frame was established by considering the stator parameters as a function of the three short-circuited windings. In [10–13], an extra branch with short-circuit-resistance was added on the fault part with shorted turns of stator windings, where the stator fault model at the d-q-0 reference frame has been further derived to separate the healthy and faulty components in the equations. In addition, [14] describes the stator fault model in the d-q-0 stationary reference frame, where the parameter changes due to faults are calculated in detail. However, the space harmonics due to the non-sinusoidal distribution of stator windings are not considered.

Most rotor fault models are based on the winding function approach, where the rotor cage is considered as a mesh that contains rotor loops (the number of rotor loops is equal to the number of rotor bars) and an end ring loop [15–17]. In [6], the steady state rotor fault was analyzed by merging the double rotor loops of the two adjacent loops, whose currents flow through the broken bar. Here, in this case, the stator current consists of the components of the main frequency and fault sidebands. Similarly, [18] analyzed the transient performance of cage induction motors under stator and rotor faults, where the rotor fault is simulated by modifying the column and row elements of the rotor loop related to the broken bar. Furthermore, [17] proposed a symmetrical components theory to simplify the analysis of the unbalance of the three-phase power system for rotor broken bar fault detection. In addition, the modeling of rotor fault was presented in [19–21] by considering a resistance ΔR_r added on the d- or q-axis rotor resistance of the healthy rotor to break the rotor symmetry at the two-phase rotor rotation axis.

Reliable stator and rotor fault models are very important to achieve online faults detection. With this consideration, this paper focuses on the dynamic modeling of stator and rotor faults. The influence of space harmonics and magnetizing saturation is investigated, which is suitable for any excited voltage and any arrangement of stator windings. The rest of the paper is organized as follows. Section 2 introduces models of healthy systems, stator and rotor faults based on the winding function method. Section 3 proposes an improved method for stator-rotor mutual inductance calculation in real-time based on the winding function and turn function distributions with respect to the rotor position. Section 4 demonstrates the simulation results of the stator and rotor faults, where the severity of stator and rotor faults under different cases are further analyzed (i.e., the torque and current spectrum analysis). Section 5 shows the experimental results on a 2.2-kW/380-V/50-Hz induction motor under healthy, stator and rotor faulty conditions, where the saturation is considered as a coefficient related to the magnetizing flux. The conclusion of this paper is presented in Section 6.

2. Stator and Rotor Fault Models

As aforementioned, the fault models are crucial for online monitoring of induction motors. For simplicity, the following assumptions are considered: (a). It is assumed that the motor is supplied by a balanced three-phase voltage source; (b) The air gap is uniformed, and the motor has no eccentricity; (c) Rotor bars are insulated to each other, and there is no inter-bar current. With those assumptions, voltage and flux expressions of a three-phase induction motor with n_b rotor bars can be derived, which will be presented in the following.

2.1. Modeling of Healthy Induction Motors

The equivalent circuit of the rotor cage is described as a mesh, which is shown in Figure 1. Here, R_b and L_b are the rotor bar resistance and leakage inductance, respectively; R_e and L_e are the resistance

and leakage inductance of the end ring segment, respectively; i_{r1} and i_{r2} represent the currents of the first and second rotor loop, respectively; i_e is the end ring current. It can be observed in Figure 1 that the arbitrary rotor loop comprises of two adjacent rotor bars, together with the end ring segments.

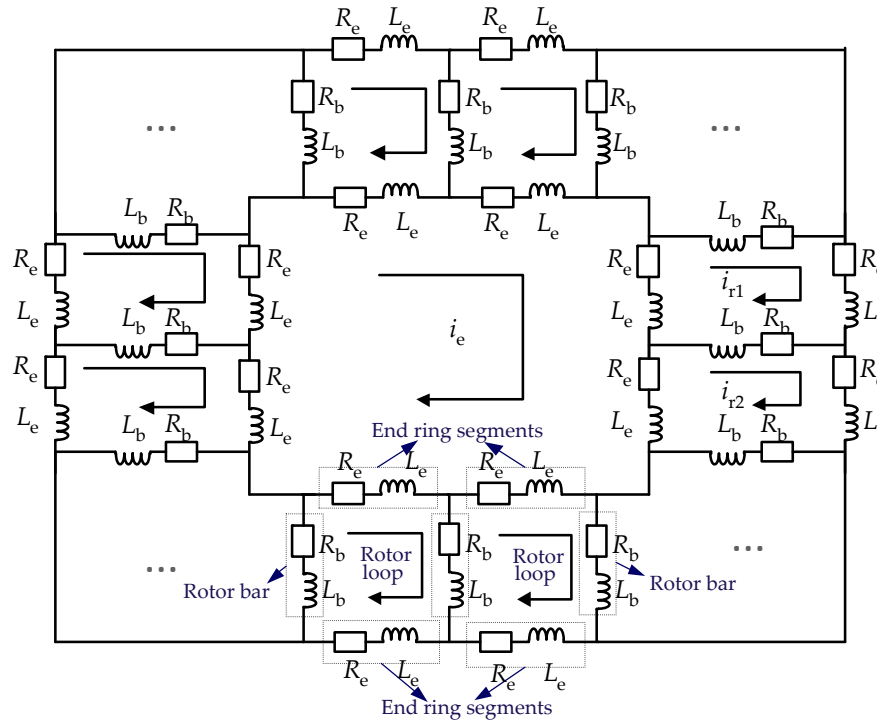


Figure 1. Equivalent circuit of the rotor cage with multiple-coupled-loops.

According to the above mesh model, the first rotor loop can be described as

$$(pL_b + R_b)(i_{r1} - i_{rn_b}) + (pL_e + R_e)i_{r1} + (pL_b + R_b)(i_{r1} - i_{r2}) + (pL_e + R_e)(i_{r1} - i_e) \quad (1)$$

where i_{rn_b} represents the current of the n_b -th rotor loop and “ p ” is the derivation operation. Then, it can be simplified as

$$(2R_b + 2R_e)i_{r1} - R_b i_{r2} - R_b i_{rn_b} - R_e i_e + p[(2L_b + 2L_e)i_{r1} - L_b i_{r2} - L_b i_{rn_b} - L_e i_e] \quad (2)$$

Next, the couplings to other rotor loops and to stator phases are considered, which leads to the following voltage equation:

$$0 = (2R_b + 2R_e)i_{r1} - R_b i_{r2} - R_b i_{rn_b} - R_e i_e + p\lambda_{r1} \quad (3)$$

$$\lambda_{r1} = [(2L_b + 2L_e)i_{r1} - L_b i_{r2} - L_b i_{rn_b} - L_e i_e] + [L_{r1sa}i_{sa} + L_{r1sb}i_{sb} + L_{r1sc}i_{sc}] + [L_{r1r1}i_{r1} + L_{r1r2}i_{r2} + \dots + L_{r1rn_b}i_{rn_b} + L_{r1e}i_e] \quad (4)$$

in which λ_{r1} is the flux of the first rotor loop, L_{r1sx} is the mutual inductance between the first rotor loop and phase x in the stator ($x = A, B, C$), L_{r1rj} is the mutual inductance of the first to j th rotor loop ($j = 1, 2, \dots, n_b$), L_{r1e} is the mutual inductance between the first rotor loop and the end ring, and $L_{r1e} = 0$.

The voltage and flux expressions of the rest rotor loops can be obtained in the same way. Moreover, for the end ring, its current does not couple with stator phases, and thus,

$$0 = n_b R_e i_e - R_e i_{r1} - R_e i_{r2} + \dots - R_e i_{rn_b} + p\lambda_e \quad (5)$$

$$\lambda_e = n_b L_e i_e - L_e i_{r1} - L_e i_{r2} - \dots - L_e i_{rn_b} \quad (6)$$

The aforementioned rotor mesh shows that there are n_b rotor loop currents and an end ring loop current, along with three-phase stator currents. There are $(n_b + 4)$ un-known currents in total for a healthy three-phase induction motor with n_b rotor bars. Therefore, the healthy motor model can be described as

(1) Voltage equations

$$\begin{cases} \mathbf{u}_{sabc} = \mathbf{R}_{sabc} \mathbf{i}_{sabc} + p \lambda_{sabc} \\ 0 = \mathbf{R}_r \mathbf{i}_r + p \lambda_r \end{cases} \quad (7)$$

where,

$$\mathbf{u}_{sabc} = \begin{bmatrix} u_{sa} \\ u_{sb} \\ u_{sc} \end{bmatrix}, \mathbf{R}_{sabc} = \begin{bmatrix} R_s & 0 & 0 \\ 0 & R_s & 0 \\ 0 & 0 & R_s \end{bmatrix}, \mathbf{i}_{sabc} = \begin{bmatrix} i_{sa} \\ i_{sb} \\ i_{sc} \end{bmatrix}, \lambda_{sabc} = \begin{bmatrix} \lambda_{sa} \\ \lambda_{sb} \\ \lambda_{sc} \end{bmatrix}$$

$$\mathbf{R}_r = \begin{bmatrix} 2(R_b + R_e) & -R_b & 0 & 0 & \dots & -R_b & -R_e \\ -R_b & 2(R_b + R_e) & -R_b & 0 & \dots & 0 & -R_e \\ 0 & -R_b & 2(R_b + R_e) & -R_b & \dots & 0 & -R_e \\ 0 & 0 & -R_b & 2(R_b + R_e) & \dots & 0 & -R_e \\ \vdots & \vdots & \vdots & \vdots & \ddots & \vdots & \vdots \\ -R_b & 0 & 0 & 0 & \dots & 2(R_b + R_e) & -R_e \\ -R_e & -R_e & -R_e & -R_e & \dots & -R_e & n_b R_e \end{bmatrix}, \mathbf{i}_r = \begin{bmatrix} i_{r1} \\ i_{r2} \\ i_{r3} \\ i_{r4} \\ \vdots \\ i_{rn_b} \\ i_e \end{bmatrix}, \lambda_r = \begin{bmatrix} \lambda_{r1} \\ \lambda_{r2} \\ \lambda_{r3} \\ \lambda_{r4} \\ \vdots \\ \lambda_{rn_b} \\ \lambda_e \end{bmatrix}$$

with R_s being the stator resistance of the symmetry stator.

(2) Flux equations

$$\begin{cases} \lambda_{sabc} = \mathbf{L}_{sabc} \mathbf{i}_{sabc} + \mathbf{L}_{sr} \mathbf{i}_r \\ \lambda_r = \mathbf{L}_r \mathbf{i}_r + \mathbf{L}_{rs} \mathbf{i}_{sabc} \end{cases} \quad (8)$$

where,

$$\mathbf{L}_{sabc} = \begin{bmatrix} L_{sasa} & L_{sasb} & L_{sasc} \\ L_{sbsa} & L_{sbsb} & L_{sbsc} \\ L_{scsa} & L_{scsb} & L_{scsc} \end{bmatrix}, \mathbf{L}_{sr} = \begin{bmatrix} L_{sar1} & L_{sar2} & L_{sar3} & L_{sar4} & \dots & L_{sarn_b} & 0 \\ L_{sbr1} & L_{sbr2} & L_{sbr3} & L_{sbr4} & \dots & L_{sbrn_b} & 0 \\ L_{scr1} & L_{scr2} & L_{scr3} & L_{scr4} & \dots & L_{scrn_b} & 0 \end{bmatrix}, \mathbf{L}_{rs} = \mathbf{L}_{sr}^T$$

$$\mathbf{L}_r = \begin{bmatrix} L_{r1r1} + 2(L_b + L_e) & L_{r1r2} - L_b & L_{r1r3} & L_{r1r4} & \dots & L_{r1rn_b} - L_b & -L_e \\ L_{r2r1} - L_b & L_{r2r2} + 2(L_b + L_e) & L_{r2r3} - L_b & L_{r2r4} - L_b & \dots & L_{r2rn_b} & -L_e \\ L_{r3r1} & L_{r3r2} - L_b & L_{r3r3} + 2(L_b + L_e) & L_{r3r4} - L_b & \dots & L_{r3rn_b} & -L_e \\ L_{r4r1} & L_{r4r2} & L_{r4r3} - L_b & L_{r4r4} + 2(L_b + L_e) & \dots & L_{r4rn_b} & -L_e \\ \vdots & \vdots & \vdots & \vdots & \ddots & \vdots & \vdots \\ L_{rn_b r1} - L_b & L_{rn_b r2} & L_{rn_b r3} & L_{rn_b r4} & \dots & L_{rn_b rn_b} + 2(L_b + L_e) & -L_e \\ -L_e & -L_e & -L_e & -L_e & \dots & -L_e & n_b L_e \end{bmatrix}$$

in which L_{sisj} is the mutual inductance between phase i and phase j ($i = a, b, c; j = a, b, c$); the way of other definitions is the same as that of the first loop. It should be noted that the stator and rotor mutual inductances depend on the rotor position during motor operation.

(3) Torque and speed equations

$$T_e = 0.5 \mathbf{i}_{sabc}^T \frac{d\mathbf{L}_{sabc}}{d\theta_m} \mathbf{i}_{sabc} + 0.5 \mathbf{i}_{sabc}^T \frac{d\mathbf{L}_{sr}}{d\theta_m} \mathbf{i}_r + 0.5 \mathbf{i}_r^T \frac{d\mathbf{L}_{rs}}{d\theta_m} \mathbf{i}_{sabc} + 0.5 \mathbf{i}_r^T \frac{d\mathbf{L}_r}{d\theta_m} \mathbf{i}_r \quad (9)$$

$$T_e = J \frac{d\omega_m}{dt} + T_L \quad (10)$$

where T_e and T_L are the electromagnetic torque and load torque, respectively, ω_m and θ_m are the mechanical angular speed and angle, respectively, and J is the inertia of the motor.

Substituting Equation (8) into (7), the healthy motor can be described by the vector given as

$$\begin{bmatrix} \mathbf{u}_{sabc} \\ 0 \end{bmatrix} = \begin{bmatrix} \mathbf{R}_{sabc} & p\mathbf{L}_{sr} \\ p\mathbf{L}_{rs} & \mathbf{R}_r \end{bmatrix} \begin{bmatrix} \mathbf{i}_{sabc} \\ \mathbf{i}_r \end{bmatrix} + \begin{bmatrix} \mathbf{L}_{sabc} & \mathbf{L}_{sr} \\ \mathbf{L}_{rs} & \mathbf{L}_r \end{bmatrix} p \begin{bmatrix} \mathbf{i}_{sabc} \\ \mathbf{i}_r \end{bmatrix} \quad (11)$$

2.2. Modeling of Stator Faults

If a stator fault is presented in the motor, an extra branch with short circuit resistance R_f will be added on the short part in the stator winding, as shown in Figure 2. The current i_f flows through the short circuit resistance R_f , and thus, the current of the fault part in the stator winding is $(i_{sa} - i_f)$ according to the Kirchhoff's current law.

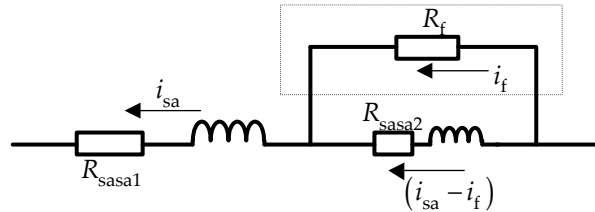


Figure 2. Representation of the stator winding inter-turn short branch.

Figure 2 further shows that the stator fault is located at phase A. The parameters related to faulted turns are considered to be proportional to the number of shorted turns n_{sf} . For example, the stator resistance of the shorted part is $k_{sf}R_s$ ($k_{sf} = n_{sf}/z_s$, and z_s is the total number of stator slots), whereas the resistance of the healthy part is $(1 - k_{sf})R_s$. Hence, the voltage equations of the stator phase A and shorted circuit are derived as

$$u_{sa} = (1 - k_{sf})R_s i_{sa} + k_{sf}R_s (i_{sa} - i_f) + d\lambda_{sa}/dt \quad (12)$$

$$R_f i_f = k_{sf}R_s (i_{sa} - i_f) + d\lambda_f/dt \quad (13)$$

Notably, other equations related to the shorted phase should be updated accordingly. As a consequence, the vector of the stator fault model can be simplified as

$$\begin{bmatrix} \mathbf{u}_{sabc} \\ 0 \\ 0 \end{bmatrix} = \begin{bmatrix} \mathbf{R}_{sabc} & \mathbf{R}_{sf} & \mathbf{pL}_{sr} \\ \mathbf{R}_{fs} & R_{ff} & \mathbf{pL}_{fr} \\ \mathbf{pL}_{rs} & \mathbf{pL}_{rf} & \mathbf{R}_r \end{bmatrix} \begin{bmatrix} \mathbf{i}_{sabc} \\ i_f \\ \mathbf{i}_r \end{bmatrix} + \begin{bmatrix} \mathbf{L}_{sabc} & \mathbf{L}_{sf} & \mathbf{L}_{sr} \\ \mathbf{L}_{fs} & L_{ff} & \mathbf{L}_{fr} \\ \mathbf{L}_{rs} & \mathbf{L}_{rf} & \mathbf{L}_r \end{bmatrix} \mathbf{p} \begin{bmatrix} \mathbf{i}_{sabc} \\ i_f \\ \mathbf{i}_r \end{bmatrix} \quad (14)$$

where $\mathbf{R}_{sf} = \begin{bmatrix} -k_{sf}R_s & 0 & 0 \end{bmatrix}^T$, $R_{ff} = -(k_{sf}R_s + R_f)$, $\mathbf{L}_{sf} = \begin{bmatrix} -k_{sf}(L_{ms} + L_{ls}) & 0.5k_{sf}L_{ms} & 0.5k_{sf}L_{ms} \end{bmatrix}^T$, $L_{ff} = -k_{sf}^2(L_{ms} + L_{ls})$, $\mathbf{L}_{fr} = k_{sf}\mathbf{L}_{sar}$ ($\mathbf{L}_{sar} = \begin{bmatrix} L_{sar1} & L_{sar2} & L_{sar3} & L_{sar4} & \dots & L_{sarn_b} & 0 \end{bmatrix}$), and $\mathbf{R}_{fs} = -\mathbf{R}_{sf}^T$, $\mathbf{L}_{fs} = -\mathbf{L}_{sf}^T$, $\mathbf{L}_{rf} = -\mathbf{L}_{fr}^T$.

2.3. Modeling of Rotor Faults

When a rotor bar broken fault is presented in the induction motor, the broken bar is removed from the loop, as shown Figure 3, where the first rotor bar is broken. It can be seen from Figure 3 that the two adjacent rotor loops surrounding the broken bar are combined into one rotor loop, and the combined loop can be described as:

$$(pL_b + R_b)(i'_{r1} - i_{rb}) + 2(pL_e + R_e)i'_{r1} + (pL_b + R_b)(i'_{r1} - i_{r3}) + 2(pL_e + R_e)(i'_{r1} - i_e) \quad (15)$$

which can be simplified as

$$(2R_b + 4R_e)i'_{r1} - R_b i_{r3} - R_b i_{rb} - 2R_e i_e + p[(2L_b + 4L_e)i'_{r1} - L_b i_{r3} - L_b i_{rb} - 2L_e i_e] \quad (16)$$

where i'_{r1} is the current of the combined rotor loop when the rotor bar broken is presented. Thus, considering the inductances, the voltage and flux equations of the combined rotor loop are described as

$$0 = (2R_b + 4R_e)i'_{r1} - R_b i_{r3} - R_b i_{rb} - 2R_e i_e + p\lambda_{r1} \quad (17)$$

$$\lambda_{r1} = [(2L_b + 4L_e)i'_{r1} - L_b i_{r3} - L_b i_{rn_b} - 2L_e i_e] + [L'_{r1sa} i_{sa} + L'_{r1sb} i_{sb} + L'_{r1sc} i_{sc}] + [L'_{r1r1} i'_{r1} + L'_{r1r3} i_{r3} + \dots + L'_{r1rn_b} i_{rn_b} + L'_{r1e} i_e] \quad (18)$$

in which L_{r1sa}' , L_{r1sb}' , L_{r1sc}' are the mutual inductance between the combined rotor loop and stator phase A, B, and C respectively, and it has relationships of $L_{r1sa}' = L_{r1sa} + L_{r2sa}$, $L_{r1sb}' = L_{r1sb} + L_{r2sb}$, $L_{r1sc}' = L_{r1sc} + L_{r2sc}$; L_{r1r1}' , L_{r1r3}' , \dots , L_{r1rn_b}' , L_{r1e}' are the self and mutual inductances of the first rotor loop, similarly, $L_{r1rj}' = L_{r1rj} + L_{r2rj}$ ($j = 1, 2, \dots$). It can be observed from Equations (17) and (18) that the voltage and flux of the combined first loop are equivalent to the case by adding the parameters of the second column and line of the parameter matrices under healthy condition to the first column and line with further simplification.

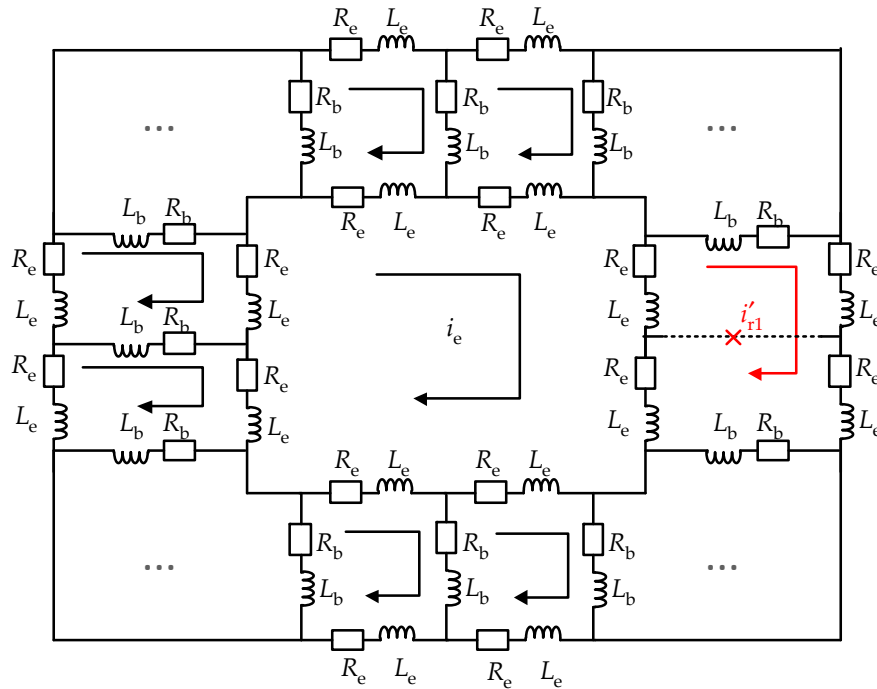


Figure 3. Representation of the rotor cage mesh when the first rotor bar is broken.

Therefore, the vector expression of the rotor broken bar model is given as

$$\begin{bmatrix} \mathbf{u}_{sabc} \\ 0 \end{bmatrix} = \begin{bmatrix} \mathbf{R}_{sabc} & p\mathbf{L}_{sr} \\ p\mathbf{L}_{rs} & \mathbf{R}_r \end{bmatrix} \begin{bmatrix} \mathbf{i}_{sabc} \\ \mathbf{i}_r \end{bmatrix} + \begin{bmatrix} \mathbf{L}_{sabc} & \mathbf{L}_{sr} \\ \mathbf{L}_{rs} & \mathbf{L}_r \end{bmatrix} p \begin{bmatrix} \mathbf{i}_{sabc} \\ \mathbf{i}_r \end{bmatrix} \quad (19)$$

where $\mathbf{i}_r = [i'_{r1} \quad i_{r3} \quad i_{r4} \quad \dots \quad i_{rn_b} \quad i_e]^T$

$$\mathbf{R}_r = \begin{bmatrix} 2(R_b + 2R_e) & -R_b & 0 & \dots & -R_b & -2R_e \\ -R_b & 2(R_b + R_e) & -R_b & \dots & 0 & -R_e \\ 0 & -R_b & 2(R_b + R_e) & \dots & 0 & -R_e \\ \vdots & \vdots & \vdots & \ddots & \vdots & \vdots \\ -R_b & 0 & 0 & \dots & 2(R_b + R_e) & -R_e \\ -2R_e & -R_e & -R_e & \dots & -R_e & n_b R_e \end{bmatrix}$$

$$\mathbf{L}_{sabc} = \begin{bmatrix} L_{sasa} & L_{sasb} & L_{sasc} \\ L_{sbsa} & L_{sbsb} & L_{sbsc} \\ L_{scsa} & L_{scsb} & L_{scsc} \end{bmatrix}, \mathbf{L}_{sr} = \begin{bmatrix} L'_{sar1} & L_{sar3} & L_{sar4} & \dots & L_{sarn_b} & 0 \\ L'_{sbr1} & L_{sbr3} & L_{sbr4} & \dots & L_{sbrn_b} & 0 \\ L'_{scr1} & L_{scr3} & L_{scr4} & \dots & L_{scrn_b} & 0 \end{bmatrix}, \mathbf{L}_{rs} = \mathbf{L}_{sr}^T$$

$$\mathbf{L}_r = \begin{bmatrix} L'_{r1r1} + 2(L_b + 2L_e) & L'_{r1r3} & L'_{r1r4} & \dots & L'_{r1rn_b} - L_b & -2L_e \\ L'_{r3r1} & L_{r3r3} + 2(L_b + L_e) & L_{r3r4} - L_b & \dots & L_{r3rn_b} & -L_e \\ L'_{r4r1} & L_{r4r3} - L_b & L_{r4r4} + 2(L_b + L_e) & \dots & L_{r4rn_b} & -L_e \\ \vdots & \vdots & \vdots & \vdots & \vdots & \vdots \\ L'_{rn_br1} - L_b & L_{rn_br3} & L_{r(n_b-1)r4} & \dots & L_{rn_brn_b} + 2(L_b + L_e) & -L_e \\ -2L_e & -L_e & -L_e & \dots & -L_e & n_b L_e \end{bmatrix}$$

2.4. Discretization

To realize the above healthy and faulty models in MATLAB/SIMULINK, the digital implementation of these models should be considered. The above derived models involve in a large amount of matrix calculations, and thus, it is necessary to find a suitable discrete method to reduce further computation cost and improve calculation accuracy. Currently, the well-known discrete methods include the first order forward/backward Euler methods, Tustin transformation, and Runge–Kutta method. Among those, the Tustin transformation not only has higher computation accuracy, but also has a lower calculation cost. It can be expressed as

$$s = \frac{2}{T_s} \frac{1 - z^{-1}}{1 + z^{-1}} \quad (20)$$

where T_s is the sampling period. Then, the model of the healthy, stator and rotor fault motors can be written as the following uniformed expression

$$\begin{aligned} \mathbf{u}(t) &= \Phi_1 \mathbf{i}(t) + \Phi_2 \frac{d}{dt} \mathbf{i}(t) \Rightarrow \\ \mathbf{u}(z) &= \Phi_1 \mathbf{i}(z) + \Phi_2 \frac{2}{T_s} \frac{1 - z^{-1}}{1 + z^{-1}} \mathbf{i}(z) \end{aligned} \quad (21)$$

with $\mathbf{u}(t)$ and $\mathbf{i}(t)$ being the voltage and current vector matrix; Φ_1 and Φ_2 representing the state matrix that depend on the models. Therefore, the discrete model is given as

$$\mathbf{i}_k = \Phi_1^{-1} \left[-\Phi_2 \mathbf{i}_{k-1} + \frac{T_s}{2} (\mathbf{u}_k + \mathbf{u}_{k-1}) \right] \quad (22)$$

in which \mathbf{i}_k and \mathbf{i}_{k-1} are the current vectors at the k th and $(k - 1)$ th steps, respectively; \mathbf{u}_k and \mathbf{u}_{k-1} are the voltage vectors at the k th and $(k - 1)$ th sampling instant.

3. Inductance Calculations

The inductances in the derived motor models are crucial for computation. The rotor bar leakage inductance L_b and end ring leakage inductance L_e can be easily calculated through the geometric parameters of the machine. The relevant inductances can be calculated by using the winding function method. The induction motor studied in this paper is a three-phase four-pole machine, which has 36 stator slots and 28 rotor bars. Each stator phase has six coils, and each coil has 42 turns, and thus, the total number of turns of one stator phase is 252 turns. According to the winding function, the inductances are calculated, which will be detailed in the following.

3.1. Stator Inductances Calculation

The turn function and winding function distribution for self and mutual inductances calculation of the stator phase A is shown in Figure 4. Furthermore, the inductances in the matrix \mathbf{L}_{sabc} can be calculated according to

$$L_{AB} = \mu_0 r l \int_0^{2\pi} n_A(\phi, \theta) F_B(\phi, \theta) g^{-1}(\phi, \theta) d\phi \quad (23)$$

which describes the inductance calculation expression of coil A to coil B. Here, in (23), μ_0 is the air gap permeability; r is the inside radius of the stator core; l is the length of the stator core; n_A is the turn

function of coil A; F_B is the winding function of coil B; g is the length of the air gap, which is constant if the eccentricity is ignored.

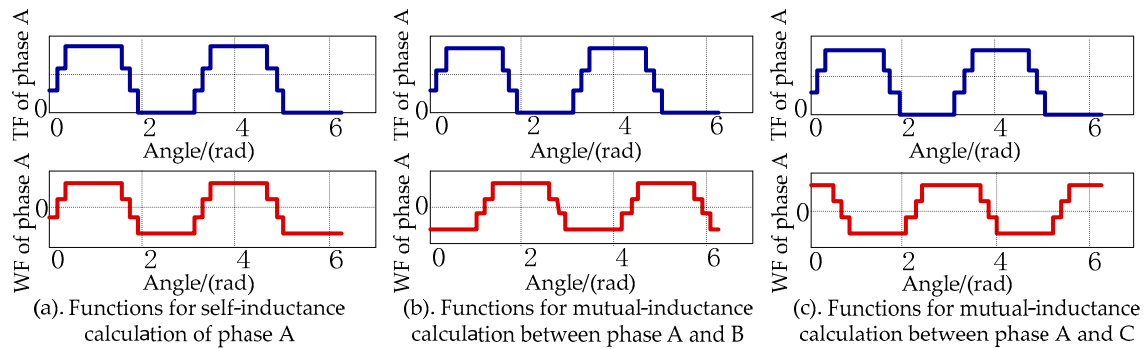


Figure 4. Turn functions (TFs) and winding functions (WFs) of stator phases.

3.2. Rotor Inductance Calculations

In order to calculate the rotor inductances, the rotor loop is taken as a coil and it has only one turn. Figure 5 presents the turn functions (TF) and winding functions (WF) for the inductance calculation of the rotor loop 1. Figure 5a shows the TF and WF of the rotor loop 1, and thus, the self-inductance can be calculated according to the TF and WF. It can be observed from Figure 5b that the winding function of the rotor loop 14 is the result of the shift of the WF of the rotor loop 1 to the right by $14 \times 2\pi/28$. Similarly, the WF of the k th rotor loop can be obtained by shifting the angle of $k \times 2\pi/28$. Hence, all the mutual inductances of rotor loops can be obtained, as shown in Figure 6, which gives the calculated inductances of the rotor loop 1. It can be observed in Figure 6 that the mutual inductances are negative, and their values are identical.

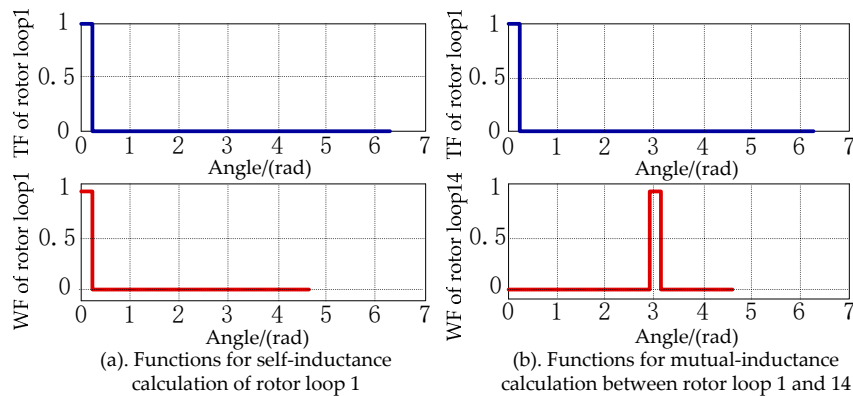


Figure 5. Turn functions (TF) and winding functions (WF) of rotor loops 1 and 14.

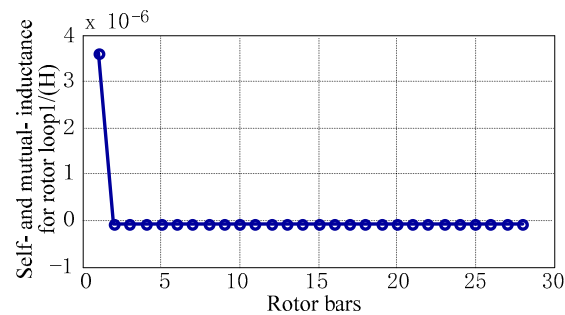


Figure 6. Inductances of the rotor loop 1.

3.3. Transient Mutual Inductance between Stator Phases and Rotor Loops Calculation

The mutual inductance calculation of stator phases to rotor loops is important, but it is difficult because the rotor position changes when the motor is running. In order to realize the real-time calculation of mutual inductances, the TF and WF with $0 \leq \theta_m < 2\pi/18 - \alpha$ are shown in Figure 7. Here, the mutual inductance can be calculated as

$$\begin{aligned}
 L_{sar1} = & \frac{\mu_0 r l}{g} \int_0^{\theta_m} N_s \left(-\frac{\alpha}{2\pi}\right) N_r d\phi + \frac{\mu_0 r l}{g} \int_{\theta_m}^{\frac{\pi}{18}} N_s \left(1 - \frac{\alpha}{2\pi}\right) N_r d\phi + \frac{\mu_0 r l}{g} \int_{\frac{\pi}{18}}^{\theta_m + \alpha} 2N_s \left(1 - \frac{\alpha}{2\pi}\right) N_r d\phi \\
 & + \frac{\mu_0 r l}{g} \int_{\theta_m + \alpha}^{\frac{2\pi}{18}} 2N_s \left(-\frac{\alpha}{2\pi}\right) N_r d\phi + \frac{\mu_0 r l}{g} \int_{\frac{2\pi}{18}}^{\frac{Q\pi}{18}} 3N_s \left(-\frac{\alpha}{2\pi}\right) N_r d\phi + \frac{\mu_0 r l}{g} \int_{\frac{Q\pi}{18}}^{\frac{(Q+1)\pi}{18}} 2N_s \left(-\frac{\alpha}{2\pi}\right) N_r d\phi \\
 & + \frac{\mu_0 r l}{g} \int_{\frac{(Q+1)\pi}{18}}^{\frac{(Q+2)\pi}{18}} N_s \left(-\frac{\alpha}{2\pi}\right) N_r d\phi + \frac{\mu_0 r l}{g} \int_{\frac{(Q+2)\pi}{18}}^{\frac{\pi}{2}} 0 \times \left(-\frac{\alpha}{2\pi}\right) N_r d\phi + \frac{\mu_0 r l}{g} \int_{\frac{\pi}{2}}^{\frac{19\pi}{18}} N_s \times \left(-\frac{\alpha}{2\pi}\right) N_r d\phi \\
 & + \frac{\mu_0 r l}{g} \int_{\frac{19\pi}{18}}^{\frac{20\pi}{18}} 2N_s \times \left(-\frac{\alpha}{2\pi}\right) N_r d\phi + \frac{\mu_0 r l}{g} \int_{\frac{20\pi}{18}}^{\frac{(Q+18)\pi}{18}} 3N_s \times \left(-\frac{\alpha}{2\pi}\right) N_r d\phi + \frac{\mu_0 r l}{g} \int_{\frac{(Q+18)\pi}{18}}^{\frac{(Q+19)\pi}{18}} 2N_s \times \left(-\frac{\alpha}{2\pi}\right) N_r d\phi \\
 & + \frac{\mu_0 r l}{g} \int_{\frac{(Q+19)\pi}{18}}^{\frac{(Q+20)\pi}{18}} N_s \times \left(-\frac{\alpha}{2\pi}\right) N_r d\phi + \frac{\mu_0 r l}{g} \int_{\frac{(Q+20)\pi}{18}}^{2\pi} 0 \times \left(-\frac{\alpha}{2\pi}\right) N_r d\phi \\
 = & \frac{\mu_0 r l N_s N_r}{g} \left(-\frac{1}{6} Q \alpha - \frac{\pi}{18} + \theta_m + 2\alpha\right)
 \end{aligned}$$

where α is the angle between two adjacent rotor slots; N_s and N_r is the number of turns of a stator and rotor coil, respectively, with $N_r = 1$; Q is the pitch of stator coil. It can be seen in Figure 7 that the position of the rotor loop 1 related to the stator phase A determines the overlapping area for the inductance calculation according to the TFs and WFs distribution. Consequently, Table 1 gives the derived mutual inductance expressions and its derivation, as a function of the rotor position. The mutual inductances between stator phases to other rotor loops are identical, as given in Table 1, but they are shifted by a certain number of angles that depend on their relative positions. For example, the mutual inductances between the stator phase B and C to the rotor loop 1 are shifted to the right by $2\pi/3$ and $4\pi/3$, respectively.

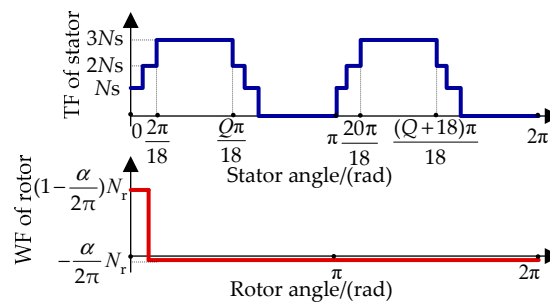


Figure 7. Turn function (TF) and winding function (WF) distribution of stator phase A to rotor loop 1 when $0 \leq \theta_m < 2\pi/18 - \alpha$.

Therefore, the mutual inductances of the rotor loop 1 to the stator phase A will be progressively in phase around the rotor periphery. Then, the mutual inductances can be obtained by using the above derivations, which can be plotted as shown in Figure 8. Furthermore, the derivation to the rotor position is shown in Figure 9.

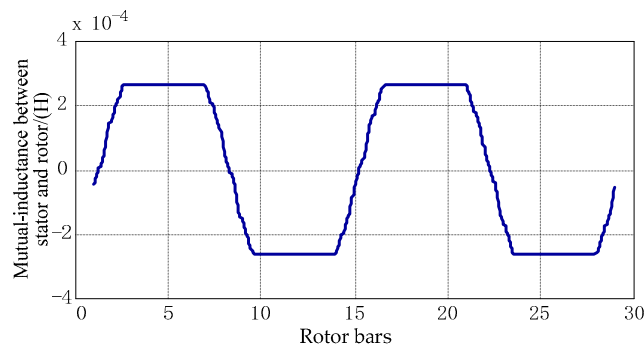


Figure 8. Mutual inductance between the stator and the rotor loop.

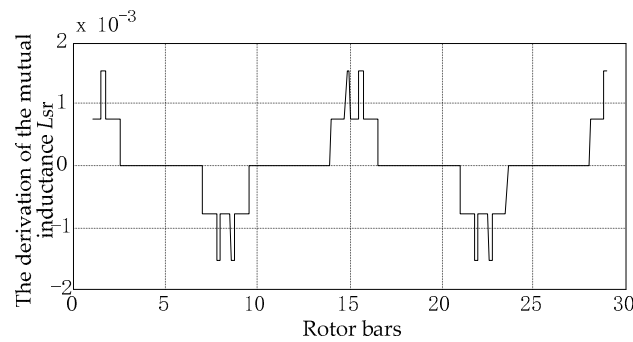


Figure 9. The derivation to the rotor position.

Table 1. Mutual inductance and its derivation with respect to rotor position.

Rotor Position	Mutual Inductance	The Derivation to Rotor Position	The Derivation to Time
$0 \leq \theta_m < 2\pi/18-\alpha$	$\frac{\mu_0 r l N_s N_r}{g} (-\frac{1}{6} Q \alpha - \frac{\pi}{18} + \theta_m + 2\alpha)$	$\frac{\mu_0 r l N_s N_r}{g}$	$\omega_m \frac{\mu_0 r l N_s N_r}{g}$
$2\pi/18-\alpha \leq \theta_m < \pi/18$	$\frac{\mu_0 r l N_s N_r}{g} (-\frac{1}{6} Q \alpha - \frac{3\pi}{18} + 2\theta_m + 3\alpha)$	$2 \frac{\mu_0 r l N_s N_r}{g}$	$2\omega_m \frac{\mu_0 r l N_s N_r}{g}$
$\pi/18 \leq \theta_m < 2\pi/18$	$\frac{\mu_0 r l N_s N_r}{g} (-\frac{1}{6} Q \alpha - \frac{2\pi}{18} + \theta_m + 3\alpha)$	$\frac{\mu_0 r l N_s N_r}{g}$	$\omega_m \frac{\mu_0 r l N_s N_r}{g}$
$2\pi/18 \leq \theta_m < Q\pi/18-\alpha$	$\frac{\mu_0 r l N_s N_r}{g} (-\frac{1}{6} Q \alpha + 3\alpha)$	0	0
$Q\pi/18-\alpha \leq \theta_m < (Q+1)\pi/18-\alpha$	$\frac{\mu_0 r l N_s N_r}{g} (-\frac{1}{6} Q \alpha + \frac{\pi}{18} - \theta_m + 2\alpha)$	$-\frac{\mu_0 r l N_s N_r}{g}$	$-\omega_m \frac{\mu_0 r l N_s N_r}{g}$
$(Q+1)\pi/18-\alpha \leq \theta_m < Q\pi/18$	$\frac{\mu_0 r l N_s N_r}{g} (-\frac{1}{6} Q \alpha + \frac{2Q+1}{18} \pi - 2\theta_m + \alpha)$	$-2 \frac{\mu_0 r l N_s N_r}{g}$	$-2\omega_m \frac{\mu_0 r l N_s N_r}{g}$
$Q\pi/18 \leq \theta_m < (Q+2)\pi/18-\alpha$	$\frac{\mu_0 r l N_s N_r}{g} (-\frac{1}{6} Q \alpha + \frac{Q+1}{18} \pi - \theta_m + \alpha)$	$-\frac{\mu_0 r l N_s N_r}{g}$	$-\omega_m \frac{\mu_0 r l N_s N_r}{g}$
$(Q+2)\pi/18-\alpha \leq \theta_m < (Q+1)\pi/18$	$\frac{\mu_0 r l N_s N_r}{g} (-\frac{1}{6} Q \alpha + \frac{2Q+3}{18} \pi - 2\theta_m)$	$-2 \frac{\mu_0 r l N_s N_r}{g}$	$-2\omega_m \frac{\mu_0 r l N_s N_r}{g}$
$(Q+1)\pi/18 \leq \theta_m < (Q+2)\pi/18$	$\frac{\mu_0 r l N_s N_r}{g} (-\frac{1}{6} Q \alpha + \frac{Q+2}{18} \pi - \theta_m)$	$-\frac{\mu_0 r l N_s N_r}{g}$	$-\omega_m \frac{\mu_0 r l N_s N_r}{g}$
$(Q+2)\pi/18 \leq \theta_m < \pi-\alpha$	$\frac{\mu_0 r l N_s N_r}{g} (-\frac{1}{6} Q \alpha)$	0	0
$\pi-\alpha \leq \theta_m < 19\pi/18-\alpha$	$\frac{\mu_0 r l N_s N_r}{g} (-\frac{1}{6} Q \alpha + \theta_m + \alpha - \pi)$	$\frac{\mu_0 r l N_s N_r}{g}$	$\omega_m \frac{\mu_0 r l N_s N_r}{g}$
$19\pi/18-\alpha \leq \theta_m < \pi$	$\frac{\mu_0 r l N_s N_r}{g} (-\frac{1}{6} Q \alpha - \frac{\pi}{18} - 2\pi + \theta_m + 2\alpha)$	$\frac{\mu_0 r l N_s N_r}{g}$	$\omega_m \frac{\mu_0 r l N_s N_r}{g}$

4. Simulation Results

To analyze the impact of stator and rotor faults, the proposed fault models are simulated on a 2.2-kW/380-V/50-Hz induction motor, whose parameters are given in Table 2. The motor is supplied by a balanced sinusoidal voltage (380-V/50-Hz). The simulation results for the stator faults and rotor faults are presented in the following section.

Table 2. Motor parameters.

Parameters	Values	Parameters	Values
l	90.2 mm	R_b	$5.9187 \times 10^{-5} \Omega$
g	0.3 mm	L_b	$4.387 \times 10^{-7} \text{ H}$
r	49 mm	R_e	$6.5 \times 10^{-6} \Omega$
R_s	2.6953Ω	L_e	$1.994 \times 10^{-8} \text{ H}$
L_{ls}	0.0113 H		

4.1. Stator Faults

Figure 10 shows the currents of the stator phases under healthy and faulty conditions. It can be observed from Figure 10a that the currents are balanced for a healthy motor. Observations of the currents in Figure 10b indicate that the magnitudes of currents are not equal. More specifically, the current magnitude of the phase B is smaller than that of the phases A and C. Furthermore, the currents in Figure 10c are notably unbalanced compared to the currents in Figure 10b, where the current of the phase B is significantly lower.

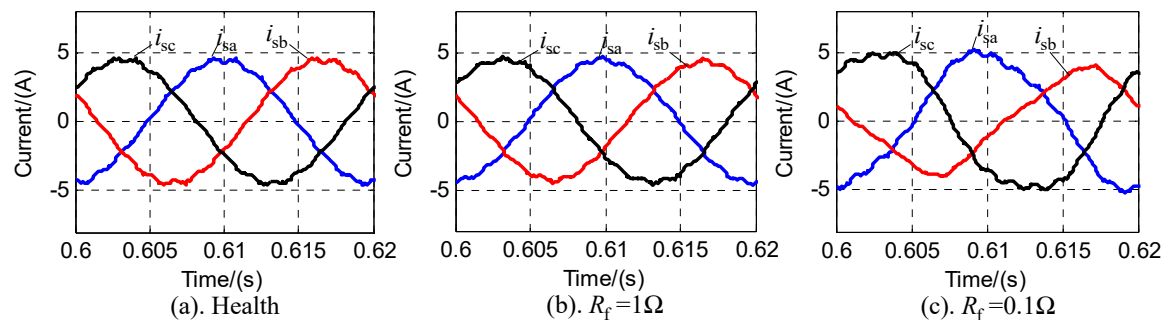


Figure 10. Currents of stator phases for 5 turns shorted stator fault with different fault resistances.

It has been reported that stator faults result in negative currents in the stator [22], which will produce $2f_1$ (f_1 is the fundamental frequency) components in the power [23] and electromagnetic torque [24]. According to the measurements, the torque is calculated and further analyzed through the fast Fourier transform (FFT) technique. Figure 11 illustrates the torque spectrum of the induction motor under healthy and stator fault conditions. It can be observed in Figure 11 that the torque magnitude at 100 Hz ($2f_1$) of the healthy motor is very small compared to the short-circuit fault motor. In addition, the torque magnitude at 100 Hz with $R_f = 0.1 \Omega$ is higher than that with $R_f = 1 \Omega$, i.e., it is less serious for a larger R_f . Therefore, it can be concluded from the simulations that the stator fault severity is related to the short circuit resistance R_f . That is, the smaller R_f is, the more serious the impact is.

Furthermore, if R_f is fixed at 0.1Ω , changing the number of shorted turns, the currents under different shorted turns can be obtained, as shown in Figure 12. Comparing the currents in Figures 12b and 12c, it can be observed that the currents in Figure 12c are unbalanced, where the current of the phases A and C in Figure 12c is increased. However, in this case, the current of the phase B is decreased, when compared with Figure 12b.

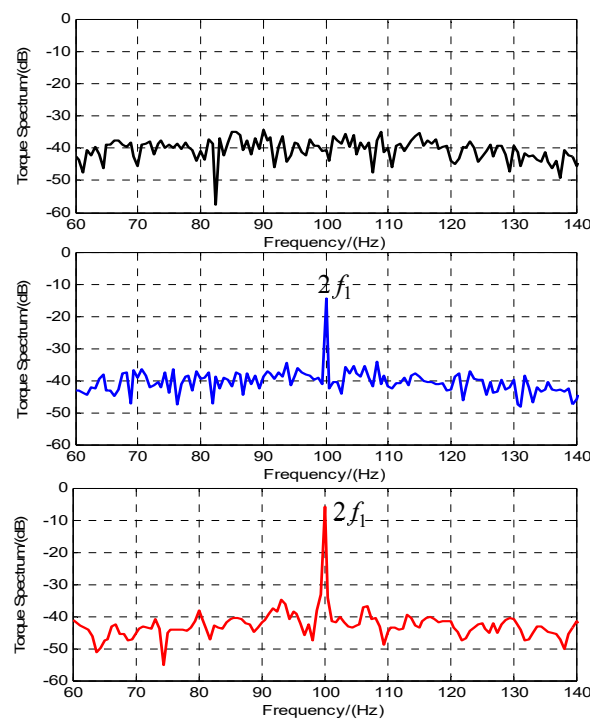


Figure 11. Torque spectrum for 5 turns shorted stator fault cases with different fault resistances (top: health, middle: $R_f = 1 \Omega$, bottom: $R_f = 0.1 \Omega$).

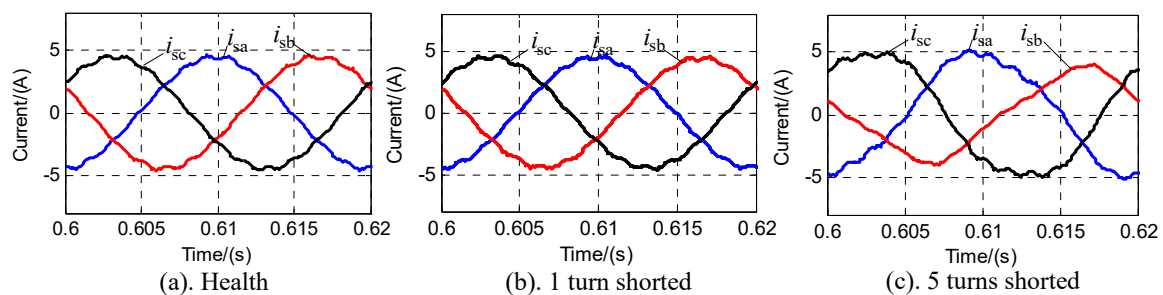


Figure 12. Currents of stator phases for $R_f = 0.1 \Omega$ with different shorted turns.

Figure 13 further shows the torque spectrum of the stator fault, where the torque magnitudes at 100 Hz ($2f_1$) of 1-turn (1T) and 5-turn (5T) shorted motors are increased compared to the healthy stator. It also can be seen in Figure 13 that the 5-turn shorted stator has a higher torque magnitude than the 1-turn shorted stator. Therefore, the stator fault severity is related to not only the short circuit resistance, but also the number of the shorted turns.

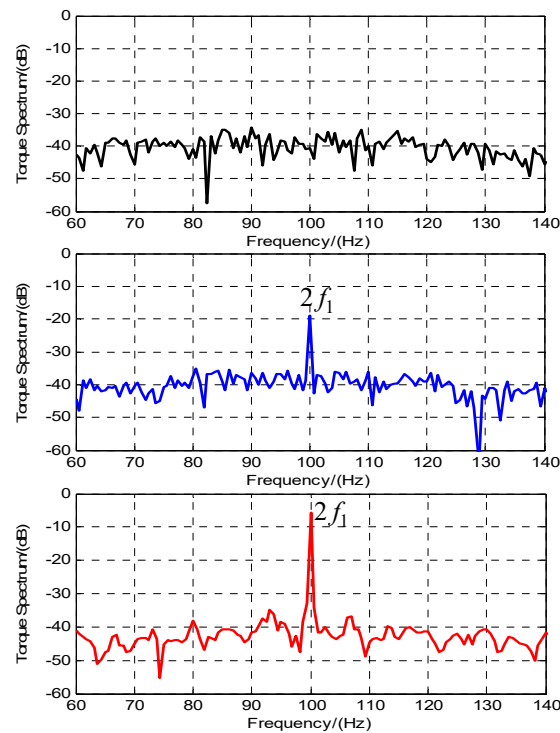


Figure 13. Torque spectrum for $R_f = 0.1 \Omega$ with different shorted turns (top: health, middle: 1 turn shorted, bottom: 5 turns shorted).

4.2. Rotor Faults

One broken rotor bar and three broken rotor bars faults are investigated in the simulation according to the above derived rotor faults model. The stator currents are shown in Figure 14. It can be observed in Figure 14 that the magnitudes of the currents of one broken rotor bar motor slightly vary in the simulation period when compared with the healthy condition. For the three broken rotor bars case, the magnitude pulsation is more obvious, as shown in Figure 14.

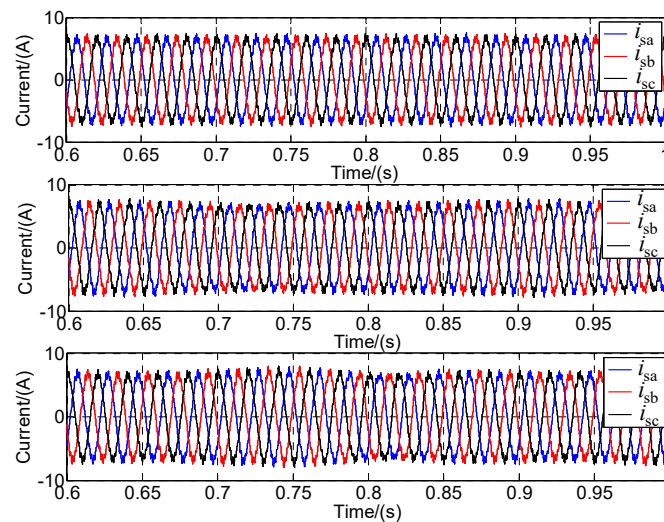


Figure 14. Stator currents of phases in the induction motor under the healthy, one broken bar and three broken bar conditions (top: health, middle: 1 broken bar, bottom: 3 broken bars).

It is proven that the rotor asymmetry can cause $(1 \pm 2s)f_1$ sidebands in the stator current [25,26], where s is the slip. The current spectrums of the healthy and broken rotor bar motors are analyzed, as

presented in Figure 15. It is indicated in Figure 15 that the $(1 \pm 2s)f_1$ component in the healthy current is negligible, while the $(1 \pm 2s)f_1$ component in the motor current of three broken rotor bars is larger than that of the one broken rotor bar. Therefore, it can be seen that the $(1 \pm 2s)f_1$ component is produced in the rotor fault, where the number of continuous broken bars determines the severity of rotor faults.

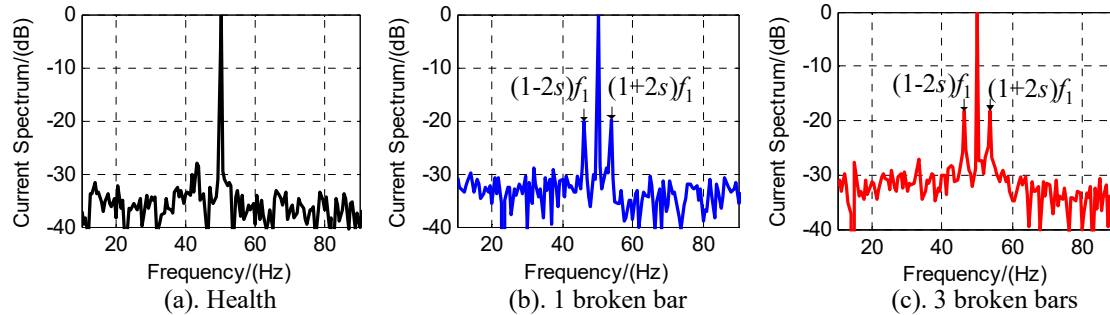


Figure 15. Current spectrums of the healthy and rotor fault motors.

5. Experimental Results

Experimental tests are performed on a 2.2-kW/380-V/50-Hz induction motor in this paper under healthy, stator and rotor faults conditions. The stator inter-turn fault motor is provided through shorting the addition taps connected to the stator coils, and the rotor broken bar fault is created by drilling holes in contiguous rotor bars. When the induction motor with the stator or rotor asymmetry is excited by the balanced sinusoidal voltage source, the motor currents and speed are measured for further analysis and assessment.

5.1. Healthy Motors

The experimental results of the stator currents are shown in Figure 16, when the balanced sinusoidal voltage is applied in the healthy induction motor. The performance is also compared with the simulation results. It can be observed from Figure 16 that the current magnitude in the experimental tests is larger than that in simulations. The difference between simulation and experimental results is due to the existence of the magnetizing saturation.

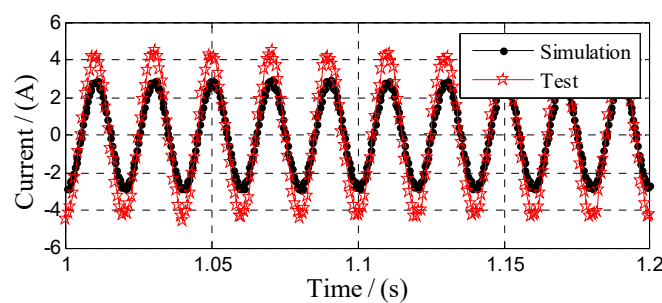


Figure 16. Comparison of simulation and experimental currents under the healthy motor condition.

More specifically, in the motor steady-state equivalent circuit, the saturation is explained as the deviation of magnetizing inductance. Thus, the saturation can be included in terms of adjusting the value of magnetizing inductance in the motor-equivalent-circuit-based model. In general, the magnetizing inductance can be described as a function of magnetizing current, in which their relationship can be fitted as a function through the measurements of no-load tests. It should be noted that the magnetizing current cannot be calculated directly.

Thus, this paper proposes to impose the magnetizing flux λ_m for the L_m calculation, and subsequently, to realize the analysis of the saturation effect in the proposed multiple-coupled-circuit models in simulations. The first step is to calculate λ_m in the simulation; then, the magnetizing current

I_m is obtained through the function of I_m and λ_m based on offline no-load tests; finally, L_m is calculated according to $L_m = \lambda_m / I_m$, and thus, k_{sat} is induced to define the coefficient of the saturation effect as

$$k_{sat} = L_m / L_{m0} \quad (24)$$

where L_m is the adjusted magnetizing inductance according to the three calculation steps; L_{m0} is the magnetizing inductance without saturation, which can be obtained using the winding function approach. Furthermore, the calculated k_{sat} is used to adjust the inductances in matrices of L_{sabc} , L_{sr} , and L_r .

The whole procedure with the consideration of saturation effect in simulations is summarized as Figure 17. When the saturation effect is considered in the models, the currents are obtained, as shown in Figure 18. It can be observed that the currents from simulations and experimental tests are well in agreement with each other. That is, the method to impose the magnetizing flux shown in Equation (24) is validated.

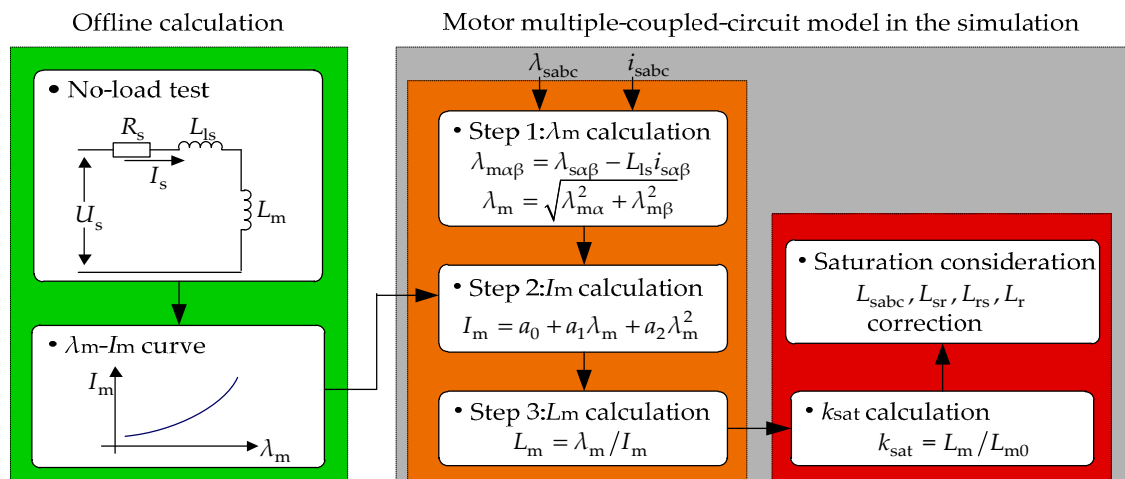


Figure 17. Procedure for inductances correction considering the saturation effect.

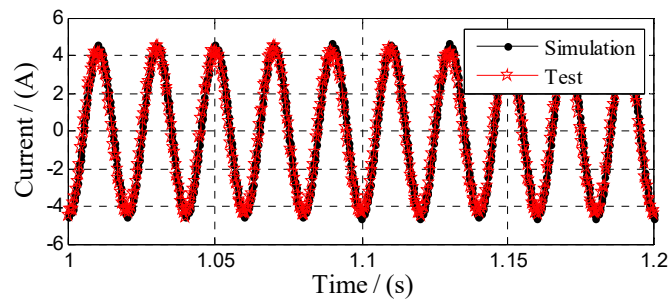


Figure 18. Simulation and experimental currents considering the magnetizing saturation.

5.2. Stator Faults

The stator currents of the five-turn shorted fault under different short circuit resistances are measured and shown in Figure 19. Figure 19a shows the appearance of the unbalance of three phase currents even for the healthy motor, which is caused by the unavoidable unbalanced three phase voltages in the experiments. When analyzing Figure 19b, it is known that there is no apparent distinction with respect to Figure 19a. In contrast, it is observed from Figure 19c that the unbalance of the currents is significant, where R_f is ten times smaller compared to Figure 19b.

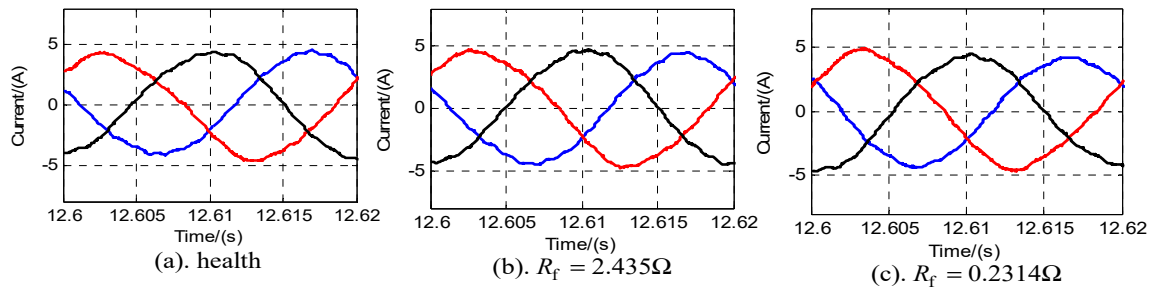


Figure 19. Stator currents of healthy, and 5-turns shorted with different short-circuit resistance in the induction motor.

In order to analyze the influence of the stator fault, the torque spectrums for the fault cases in Figure 19 are presented in Figure 20. It can be observed that the torque magnitude at 100 Hz ($2f_1$) for the healthy motor is comparatively high because of the unbalanced voltage. Moreover, the torque magnitudes at 100 Hz under the stator faults are larger than that under the healthy condition. In addition, it also can be seen in Figure 19 that the lower the short circuit resistance is, the higher the torque magnitude at 100 Hz in the torque spectrum will be.

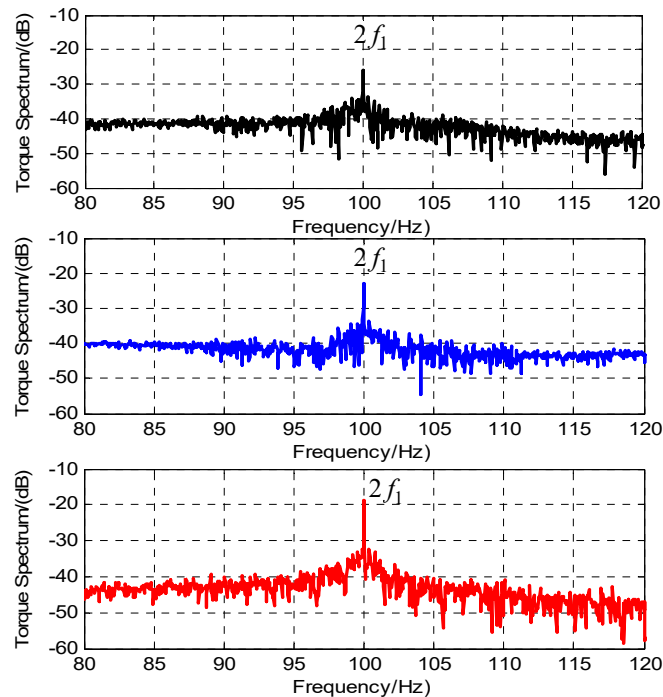


Figure 20. Torque spectrum under stator faults (top: health, middle: $R_f = 2.435 \Omega$, bottom: $R_f = 0.2314 \Omega$).

The measured currents are then compared considering the different number of shorted turns with $R_f = 0.1 \Omega$, and the torque spectrums are further analyzed, as shown in Figures 21 and 22, respectively. It can be observed from Figures 21 and 22 that the degree of unbalance or the torque magnitude of 100 Hz increases with the increasing of the number of shorted turns.

When comparing with the simulation results in Figures 10–13, it is known that the experimental results agree with the simulation results. Then, it can be concluded that the stator fault severity is related to the short circuit resistance and the number of shorted turns. The lower the short circuit resistance is or the higher the number of the shorted turns is, the more serious the stator inter-turn fault will become.

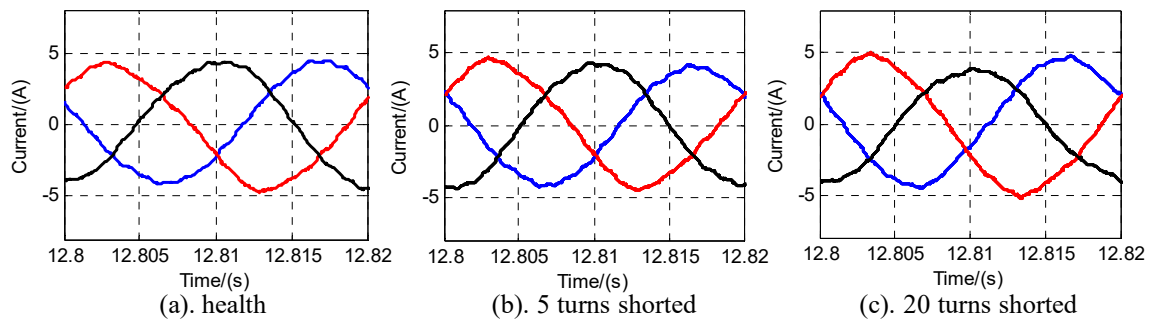


Figure 21. Stator currents of different shorting turns with $R_f = 0.1 \Omega$ in the induction motor.

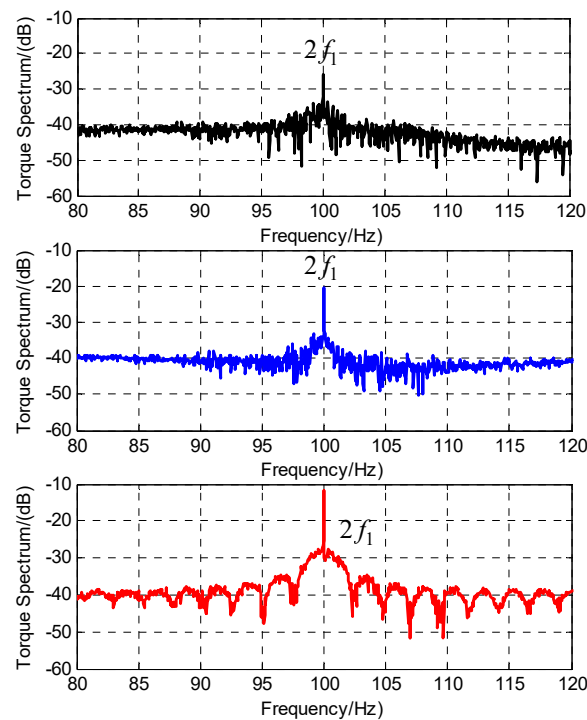


Figure 22. Torque spectrum under stator faults (top: health, middle: 5 turns shorted, bottom: 20 turns shorted).

5.3. Rotor Faults

When the rotor with broken bars in the motor is considered, the currents are measured and shown in Figure 23. Similarly, the current spectrum is analyzed, as shown in Figure 23. It can be seen in Figures 23 and 24 that the $(1 \pm 2s)f_1$ component in the stator current is produced in the rotor fault motor, where the current magnitude at $(1 \pm 2s)f_1$ of the three broken bars rotor is larger than that of the one broken bar rotor.

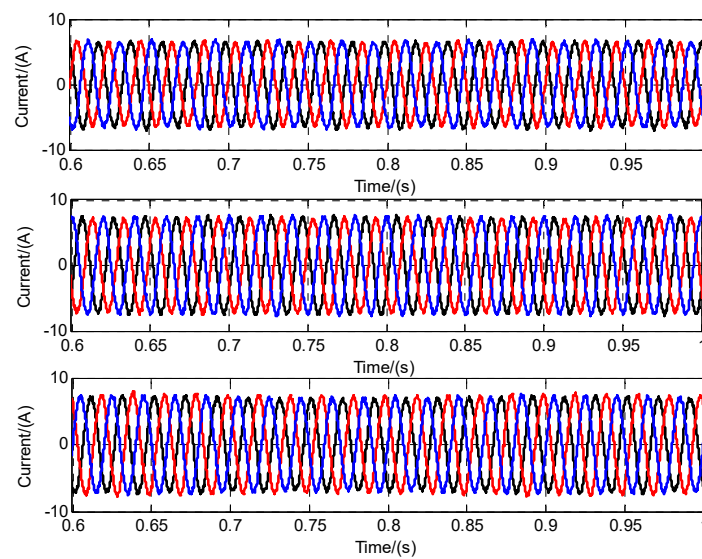


Figure 23. Motor currents under rotor faults (top: health, middle: 1 broken bar, bottom: 3 broken bars).

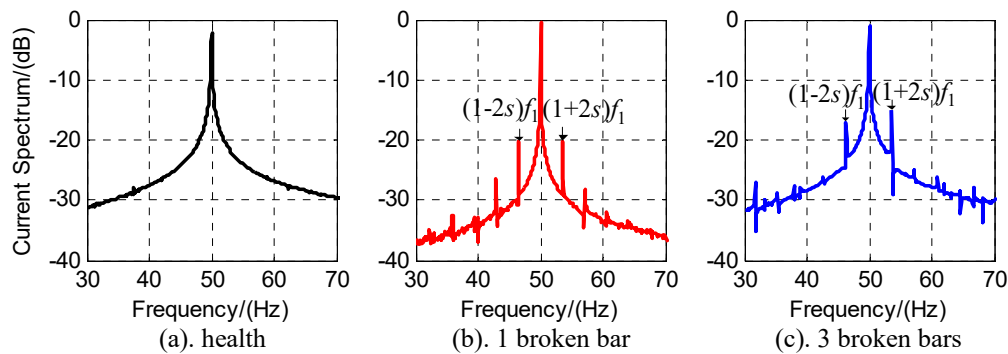


Figure 24. Current spectrums under rotor faults.

6. Conclusions

In this paper, stator and rotor fault models considering the saturation effect were proposed based on the winding function approach. The stator and rotor mutual inductances are crucial for the models, and hence, how to calculate the inductance in real-time according to the proposed models was detailed in this paper. Furthermore, the discrete model was obtained through the Tustin transformation for digital implementation, where a uniform model was given to describe the motor model under healthy and faulty conditions. Simulation and experimental results have demonstrated the effectiveness of the proposed model, where the $2f_1$ -frequency components in the torque and $(1 - 2s)f_1$ -frequency components in the current were considered to assess the fault severity under various faulty cases. It can be concluded from the simulation and experimental results that the stator fault severity is related to the short circuit resistance and the number of shorted turns. Moreover, the larger the number of continuous broken bars is, the more serious the rotor faults will be. In all, the proposed models can be used to provide stator and rotor fault information in simulations with the consideration of the saturation effect, which in turn enables the evaluation of the fault severity of the induction motor.

Author Contributions: All authors contributed equally to this paper, where the first and corresponding authors were responsible for the conceptualization, the first author also for methodology, validation, writing, and other authors mainly for writing. All authors have read and agreed to the published version of the manuscript.

Funding: This research was funded by the Fundamental Research Funds for the Central Universities (2018JBZ004).

Acknowledgments: The author would like to thank the editor and the reviewers who provided many helpful comments and thereby contributed to the final manuscript.

Conflicts of Interest: The authors declare no conflict of interest.

References

1. Motor Reliability Working Group. Report of large motor reliability survey of industrial and commercial installations, part I. *IEEE Trans. Ind. Appl.* **1985**, *1*, 865–872. [CrossRef]
2. Nguyen, V.; Wang, D.; Seshadrinath, J.; Ukil, A.; Krishna, M.S.; Nadarajan, S.; Vaiyapuri, V. A Method for Incipient Interturn Fault Detection and Severity Estimation of Induction Motors under Inherent Asymmetry and Voltage Imbalance. *IEEE Trans. Transp. Electr.* **2017**, *3*, 703–715. [CrossRef]
3. Khezzar, A.; Oumaamar, M.E.K.; Hadjami, M.; Boucherma, M.; Razik, H. Induction Motor Diagnosis Using Line Neutral Voltage Signatures. *IEEE Trans. Ind. Electron.* **2009**, *56*, 4581–4591. [CrossRef]
4. Malekpour, M.; Phung, B.T.; Ambikairajah, E. Online technique for insulation assessment of induction motor stator windings under different load conditions. *IEEE Trans. Dielectr. Electr. Insul.* **2017**, *24*, 349–358. [CrossRef]
5. Toliyat, H.A.; Nandi, S.; Choi, S.; Meshgin-Kelk, H. *Electric Machines: Modeling, Condition Monitoring, and Fault Diagnosis*; CRC Press LLC: Boca Raton, FL, USA, 2012; ISBN 978-0-8493-7027-4.
6. Williamson, S.; Smith, A.C. Steady-state analysis of 3-phase cage motors with rotor-bar and end-ring faults. *IEE Proc. B Electr. Power Appl.* **1982**, *129*, 93. [CrossRef]
7. Rahman, M.M.; Uddin, M.N. Online Unbalanced Rotor Fault Detection of an IM Drive Based on Both Time and Frequency Domain Analyses. *IEEE Trans. Ind. Appl.* **2017**, *53*, 4087–4096. [CrossRef]
8. Williamson, S.; Mirzoian, K. Analysis of Cage Induction Motors with Stator Winding Faults. *IEEE Trans. Power Appl. Syst.* **1985**, *PAS-104*, 1838–1842. [CrossRef]
9. Chang, X.; Cocquempot, V.; Christophe, C. A model of asynchronous machines for stator fault detection and isolation. *IEEE Trans. Ind. Electron.* **2003**, *50*, 578–584. [CrossRef]
10. Cruz, S.M.A.; Cardoso, A.J.M. The method of multiple reference frames applied to the diagnosis of stator faults in three-phase induction motors. In Proceedings of the 4th International Power Electronics and Motion Control Conference, Xi'an, China, 14–16 August 2004; Volume 2, pp. 603–609. Available online: <http://ieeexplore.ieee.org/stamp/stamp.jsp?tp=&arnumber=1375635&isnumber=30039> (accessed on 14 August 2018).
11. Cruz, S.M.A.; Cardoso, A.J.M. Multiple reference frames theory: A new method for the diagnosis of stator faults in three-phase induction motors. *IEEE Trans. Energy Convers.* **2005**, *20*, 611–619. [CrossRef]
12. Cruz, S.M.A.; Toliyat, H.A.; Cardoso, A.J.M. DSP Implementation of the Multiple Reference Frames Theory for the Diagnosis of Stator Faults in a DTC Induction Motor Drive. *IEEE Trans. Energy Convers.* **2005**, *20*, 329–335. [CrossRef]
13. Tallam, R.M.; Habetler, T.G.; Harley, R.G. Transient model for induction machines with stator winding turn faults. *IEEE Trans. Ind. Appl.* **2002**, *38*, 632–637. [CrossRef]
14. Patel, D.C.; Chandorkar, M.C. Modeling and Analysis of Stator Interturn Fault Location Effects on Induction Machines. *IEEE Trans. Ind. Electron.* **2014**, *61*, 4552–4564. [CrossRef]
15. El Bouchikhi, E.H.; Choqueuse, V.; Benbouzid, M. Induction machine faults detection using stator current parametric spectral estimation. *Mech. Syst. Signal Process.* **2015**, *52*, 447–464. [CrossRef]
16. Jung, J.; Kwon, B. Corrosion Model of a Rotor-Bar-Under-Fault Progress in Induction Motors. *IEEE Trans. Ind. Electron.* **2006**, *53*, 1829–1841. [CrossRef]
17. Jerkan, D.G.; Reljić, D.D.; Marčetić, D.P. Broken Rotor Bar Fault Detection of IM Based on the Counter-Current Braking Method. *IEEE Trans. Energy Convers.* **2017**, *32*, 1356–1366. [CrossRef]
18. Toliyat, H.A.; Lipo, T.A. Transient analysis of cage induction machines under stator, rotor bar and end ring faults. *IEEE Trans. Energy Convers.* **1995**, *10*, 241–247. [CrossRef]
19. Cruz, S.M.A.; Stefani, A.; Filippetti, F.; Cardoso, A.J.M. A New Model-Based Technique for the Diagnosis of Rotor Faults in RFOC Induction Motor Drives. *IEEE Trans. Ind. Electron.* **2009**, *55*, 4218–4228. [CrossRef]
20. Toscani, S.; Faifer, M.; Rossi, M.; Cristaldi, L.; Lazzaroni, M. Effects of the Speed Loop on the Diagnosis of Rotor Faults in Induction Machines. *IEEE Trans. Instrum. Meas.* **2012**, *61*, 2713–2722. [CrossRef]
21. Cruz, S.M.A. An Active—Reactive Power Method for the Diagnosis of Rotor Faults in Three-Phase Induction Motors Operating Under Time-Varying Load Conditions. *IEEE Trans. Energy Convers.* **2012**, *27*, 71–84. [CrossRef]

22. Bouzid, M.B.K.; Champenois, G. New Expressions of Symmetrical Components of the Induction Motor Under Stator Faults. *IEEE Trans. Ind. Electron.* **2013**, *60*, 4093–4102. [[CrossRef](#)]
23. Drif, M.; Cardoso, A.J.M. Stator Fault Diagnostics in Squirrel Cage Three-Phase Induction Motor Drives Using the Instantaneous Active and Reactive Power Signature Analyses. *IEEE Trans. Ind. Inform.* **2014**, *10*, 1348–1360. [[CrossRef](#)]
24. Siddique, A.; Yadava, G.S.; Singh, B. A review of stator fault monitoring techniques of induction motors. *IEEE Trans. Energy Convers.* **2005**, *20*, 106–114. [[CrossRef](#)]
25. Pons-Llinares, J.; Antonino-Daviu, J.A.; Riera-Guasp, M.; Bin Lee, S.; Kang, T.; Yang, C. Advanced Induction Motor Rotor Fault Diagnosis via Continuous and Discrete Time–Frequency Tools. *IEEE Trans. Ind. Electron.* **2015**, *62*, 1791–1802. [[CrossRef](#)]
26. Antonino-Daviu, J.A.; Quijano-López, A.; Rubbiolo, M.; Climente-Alarcon, V. Advanced Analysis of Motor Currents for the Diagnosis of the Rotor Condition in Electric Motors Operating in Mining Facilities. *IEEE Trans. Ind. Appl.* **2018**, *54*, 3934–3942. [[CrossRef](#)]



© 2019 by the authors. Licensee MDPI, Basel, Switzerland. This article is an open access article distributed under the terms and conditions of the Creative Commons Attribution (CC BY) license (<http://creativecommons.org/licenses/by/4.0/>).